RSC Advances

PAPER

View Article Online
View Journal | View Issue

Cite this: *RSC Adv.*, 2017, **7**, 20027

Ultra high stable supercapacitance performance of conducting polymer coated MnO_2 nanorods/rGO nanocomposites†

K. Hareesh, *[ab] B. Shateesh,[c] R. P. Joshi,[b] J. F. Williams,[a] D. M. Phase,[d] S. K. Haram*[c] and S. D. Dhole*[b]

Received 11th February 2017
Accepted 29th March 2017

DOI: 10.1039/c7ra01743j

rsc.li/rsc-advances

A ternary nanocomposite that consists of MnO_2 nanorods and reduced graphene oxide sheets supported on poly(3,4-ethylenedioxythiophene)-poly(styrenesulfonate) (PEDOT:PSS) polymer has been developed for supercapacitor applications. X-ray diffraction, field emission scanning electron microscopy, Raman spectroscopy, X-ray photoelectron spectroscopy, the Brunauer–Emmett–Teller method and X-ray photoelectron spectroscopic analysis confirmed the formation of a ternary nanocomposite of PEDOT:PSS/MnO_2 nanorods/rGO. Electrochemical investigation of these materials in acetonitrile containing lithium per chlorate demonstrated an enhanced specific capacitance of 633 F g^{-1} at a current density of 0.5 A g^{-1} and 100% stability up to 5000 charging–discharging cycles at 1 A g^{-1}. The enhanced capacitance and working stability of the PEDOT:PSS/MnO_2 nanorods/rGO nanocomposite along with the simplicity in making the active materials make this system a promising candidate for the commercial development of supercapacitors.

Introduction

Transition metal oxides have attracted immense attention because of their applications in various fields such as active materials for water splitting catalysts, sensors, pollutant degradation, Li-ion batteries, supercapacitors, *etc.*[1,2] Supercapacitors are alternative energy storage-conversion devices that show rapid charging–discharging rates, a high power density and a long cycle life. Supercapacitors have a variety of applications, such as in memory backup systems, industrial power, consumer electronics, public transportation and military devices.[3–5] Among various transition metal oxides, MnO_2 has received tremendous attention due to its low cost, environmental friendliness and natural abundance.[6] α-MnO_2 is a polymorph of MnO_2 with different spatial arrangements depending upon linkage of its basic MnO_6 octahedral units.[7] However, its low inherent electrical conductivity (10^{-5} to 10^{-6} S cm^{-1}) is a main constraint for its widespread application.[8] Overcoming this limitation has been attempted by combining it with carbon based materials, such as graphene/reduced graphene oxide, to improve its conductivity.[9,10]

Graphene is a layer polymorph of carbon with a 2D hexagonal packing layered structure and can offer a useful synergy by serving both as a conducting agent and as the cathode material.[11,12] Reduced graphene oxide (rGO) is considered a physical analogue of graphene that can be obtained by reducing the oxygen functional groups present on the edge and basal plane of graphene oxide (GO) and is considered to be a cost effective substitute for graphene prepared by physical methods.[13,14]

Recently, researchers have demonstrated many binary systems with the combination of different kinds of MnO_2 and rGO/carbon nanotube (CNT). Zhao *et al.*[15] have reported the uniform anchoring of MnO_2 nanosheets on macroporous graphene for supercapacitor electrodes. Xia *et al.*[16] have studied a MnO_2–CNT nanocomposite and observed an enhancement in supercapacitance compared to the individual MnO_2 and CNT components. The carbon nanofibres/MnO_2 nanosheets have been synthesized for an asymmetric supercapacitance application by Ning *et al.*[17] Bristle-like α-MnO_2 has been grown on multi-walled CNTs by Vinny *et al.*[18] for asymmetric supercapacitance applications. Ma *et al.*[19] have synthesized hierarchical MnO_2 nanowire/graphene hybrid fibres with excellent electrochemical performance. Liu *et al.*[20] have reported the *in situ* chemical synthesis of sandwich structured MnO_2/graphene nanoflowers for supercapacitive applications. A three dimensional pompon-like MnO_2/graphene hydrogel composite has been synthesized by Zhang *et al.*[21] for supercapacitor applications.

[a]*School of Physics, University of Western Australia, Crawley, WA 6009, Australia. E-mail: appi.2907@gmail.com*

[b]*Department of Physics, Savitribai Phule Pune University, Pune – 411007, India. E-mail: sanjay@physics.unipune.ac.in*

[c]*Department of Chemistry, Savitribai Phule Pune University, Pune – 411007, India. E-mail: haram@chem.unipune.ac.in*

[d]*UGC-DAE Consortium for Scientific Research, Indore – 452001, India*

† Electronic supplementary information (ESI) available: The EDS analysis for the MnO_2 nanorods, and the MG and MGP nanocomposites. XRD of graphene oxide. TGA of graphene oxide, MnO_2, and the MG and MGP nanocomposites. See DOI: 10.1039/c7ra01743j

The specific capacitance of these binary nanocomposites can be further enhanced by combining them with a conducting support like *viz.* PEDOT:PSS, polyaniline, polypyrrole, *etc.*[22] Among many conducting polymers, the PEDOT:PSS polymer has received attention due to its easy processability and its conjugated backbone, which allows an easy conveyance of delocalized electrons through the π orbital system.[23–26] The unfilled valence shells of oxygen atoms in PEDOT:PSS act as doping levels that make it important in charge storage materials.[27] A plausible reason for this enhancement might be due to the dispersion of binary active materials in the conducting matrix, which may allow all the edges and the corners to be available for charge storage as well as protect the faradic materials from dissolution into the electrolyte. Supercapacitance applications for a graphene/MnO_2 nanostructure wrapped by the PEDOT:PSS polymer have been studied by Yu *et al.*[28] Hou *et al.*[29] have improved the specific capacitance of MnO_2 nanospheres/CNT nanocomposites by wrapping them with the PEDOT:PSS conducting polymer. The sandwich-structure MnO_2/polypyrrole/rGO hybrid composites have been synthesized by Han *et al.*[30] for high performance supercapacitors. The same research group synthesized a combination of MnO_2 nanorods/GO nanocomposites and polyaniline to enhance the supercapacitance performance.[31] Pan *et al.*[32] have reported the two step synthesis of polyaniline/MnO_2/graphene ternary composites for electrochemical supercapacitor applications. The glycol assisted synthesis of a graphene–MnO_2–polyaniline ternary nanocomposite for supercapacitor applications has been studied by Mu *et al.*[33] Li *et al.*[34] synthesized the MnO_2 nanoflakes/polyaniline nanorods hybrid nanostructures on graphene paper and observed tan enhancement in supercapacitance performance. The electrochemical properties of the MnO_2 nanosheet array/rGO/PEDOT:PSS ternary composite electrode material for supercapacitor applications has been studied by Yan *et al.*[35] These composites showed a capacitance retention of 66.2% over 2000 cycles. A decrease in the capacitance retention has been attributed to the dissolution of the MnO_2 counterpart into the aqueous electrolyte during cycling. They used a simple sonication method to coat PEDOT:PSS on MnO_2/rGO, which perhaps is not enough to coat PEDOT:PSS firmly on MnO_2/rGO. Therefore, an alternative approach is needed to coat the PEDOT:PSS polymer on the MnO_2/rGO nanocomposite in which the PEDOT:PSS will be coated firmly on MnO_2/rGO and prevent dissolution. With this motivation, we developed an alternative chemical approach to coat PEDOT:PSS on MnO_2. Besides, to forbid the dissolution we replaced the aqueous electrolyte by organic solvents, which have been found to play a positive role in imparting the outstanding cycling stability.

Herein, we prepared MnO_2/rGO composites with hydrothermal methods and the formation of nanorods of MnO_2 have been noted in the product. These have been coated successfully with PEDOT:PSS by chemical routes that result in a ternary composite ready for supercapacitor applications. These materials have been characterized thoroughly and their supercapacitance performance has been studied by cyclic voltammetry, galvanostatic charge–discharge cycling and electrochemical impedance spectroscopy in acetonitrile solution containing 1 M lithium perchlorate ($LiClO_4$).

Experimental details

Potassium permanganate ($KMnO_4$), sulfuric acid (H_2SO_4), PEDOT:PSS, polyvinylidene fluoride (PVDF), acetonitrile and $LiClO_4$ were procured from Sigma-Aldrich. All the other chemicals used were analytical grade unless specified. Milli-Q® (MQ) water was used throughout the experiments.

Synthesis of nanocomposites

GO was synthesized by a modified Hummers' method and the procedure is explained elsewhere.[36] The MnO_2/rGO nanocomposite was prepared by a hydrothermal method and the procedure used is as follows. The synthesized GO was dispersed in double distilled water with a concentration of 1 mg ml^{-1} and sonicated for an hour. 0.3 g of $KMnO_4$ was added to it and it was stirred for another hour. The mixture was transferred into a Teflon lined autoclave. The autoclave was sealed and heated in an oven at 150 °C for 6 h. After cooling, the product was collected by centrifugation, washed with MQ water, dried overnight at 100 °C, and named as MG nanocomposite. For the preparation of the PEDOT:PSS/MnO_2/rGO nanocomposite, two steps were employed. The MnO_2/rGO nanocomposite was synthesized as explained above. It was then dispersed in 50 ml of MQ water with concentration of 2 mg ml^{-1} and subsequently heated with vigorous stirring. Once the temperature reached 80 °C, 5 ml of PEDOT:PSS was added and stirred for an hour at the same temperature. After cooling to room temperature, the product was centrifuged, washed with MQ water, dried overnight, and named as MGP nanocomposite. MnO_2 nanorods were synthesized by adding 0.3 g of $KMnO_4$ and 0.2 ml H_2SO_4 in 25 ml of MQ water and keeping the remaining conditions same as above.

Characterization of the nanocomposites

The surface morphologies of the prepared nanocomposites along with the MnO_2 nanorods and GO have been determined using field emission scanning electron microscopy (FESEM, Model Nova Nanosem 450) and EDAX analysis (using Bruker XFlash 6130). The structural analysis was done using an X-ray diffractometer having a CuK_α source (model Bruker AXS D8 Advance). XPS was performed using an Omicron EA 125 analyser at room temperature in an ultrahigh vacuum chamber. Raman measurements were done with a Renishaw Invia laser Raman microscope with a laser excitation wavelength of 532 nm. A Brunauer–Emmett–Teller (BET) analyser (model Quantachrome, Model Autosorb iQ2) was used to study the surface area, pore size and pore diameter by nitrogen gas absorption–desorption.

Electrochemical analysis of the nanocomposites

The electrochemical analysis of the nanocomposites was performed using a BioLogic potentiostat (model: SP 300) workstation with a three-electrode system in acetonitrile solution containing 1 M $LiClO_4$ with platinum wire as a counter electrode

and silver wire as a quasi-reference electrode. The working electrodes were prepared by mixing the nanocomposites, carbon block and PVDF (1% wt) in NMP with a mass ratio of 70 : 20 : 10. This mixture was loaded on a carbon flag having a geometrical area of 1 cm^2 and the active mass of the electrode was ~7% wt (0.3 mg). Cyclic voltammetry (CV) in the range 0–1.1 V was performed at varied scan rates. The galvanostatic charge/discharge (CD) tests for all the nanocomposites were carried out in the potential range of 0–1.1 V at varied current densities. The electrochemical impedance spectra (EIS) were recorded in a frequency range from 6 MHz to 200 mHz.

Results and discussion

The synthesis of the MGP nanocomposite includes two steps; the first one is the preparation of the MG nanocomposite by a hydrothermal method and the next is coating PEDOT:PSS polymer over that to obtain the MGP nanocomposite.

The $KMnO_4$ used in the reaction is dissociated and forms nanocrystalline MnO_2 as follows,[16]

$$4MnO_4^- + 2H_2O \rightarrow 4MnO_2 + 4OH^- + 3O_2 \quad (1)$$

During the hydrothermal reaction, these formed MnO_2 nanocrystallites may serve as nucleation sites. The newly formed MnO_2 nanocrystallites could deposit on pre-formed MnO_2 nanocrystallites and form MnO_2 nanorods. Simultaneously, GO will also be reduced into rGO by the removal of oxygen functional groups.[37] The flower like morphology of the MG nanocomposite may be due to the preferred growth of the MnO_2 nanorods on rGO. The formed MG nanocomposite was mixed with the PEDOT:PSS conducting polymer and heated at 80 °C. During heating, the conducting polymer coated the MG nanocomposite and acts as a supporting layer.[22] The schematic representation of the synthesis of the MGP nanocomposite is shown in Scheme 1.

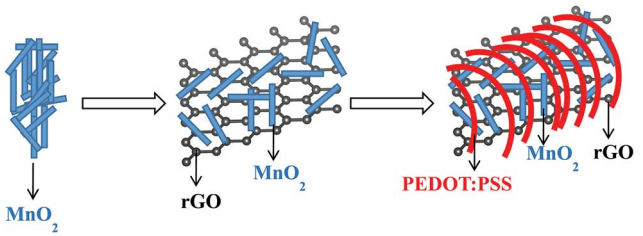

Scheme 1 A schematic diagram of the preparation of the MGP nanocomposite.

Fig. 1 depicts FESEM images of GO, MnO_2 nanorods, and MG and MGP nanocomposites. Fig. 1(a) depicts the homogeneous composition of GO and Fig. 1(b) depicts MnO_2 nanorods having a diameter in the range 10–75 nm. Fig. 1(c) shows the decoration of MnO_2 nanorods on rGO sheets and they are seen in the form of flower like structures having a diameter of ~825 nm (shown in the inset of Fig. 1(c)). However, these structures are not legible in the MGP nanocomposite (Fig. 1(d)) as they are coated by the PEDOT:PSS polymer. Fig. 2 shows an elemental mapping of the MnO_2 nanorods, and the MG and MGP nanocomposites. It can be seen from Fig. 2 that the elements Mn, O, C and S are uniformly distributed, confirming the presence of MnO_2 and PEDOT:PSS polymer in the nanocomposites. The presence of Mn, C, O and S in the nanocomposites is also confirmed by EDS of the MnO_2 nanorods, and the MG and MGP nanocomposites, shown in Fig. S1 (ESI†).

Fig. 3(a) shows the XRD of MnO_2 nanorods, and the MG and MGP nanocomposites. The XRD for GO is shown in Fig. S2 (ESI†). MnO_2 nanorods showed peaks at 18.12°, 28.75°, 37.51°, 41.89°, 49.9°, 56.18°, 59.99°, 65.33°, and 69.33° corresponding to the Miller indices (200), (310), (211), (301), (411), (600), (521), (002), (541), respectively, indicating the formation of a tetragonal phase of α-MnO_2 nanorods[10] and is in agreement with JCPDF file no 44-0141. The respective peaks are also observed in

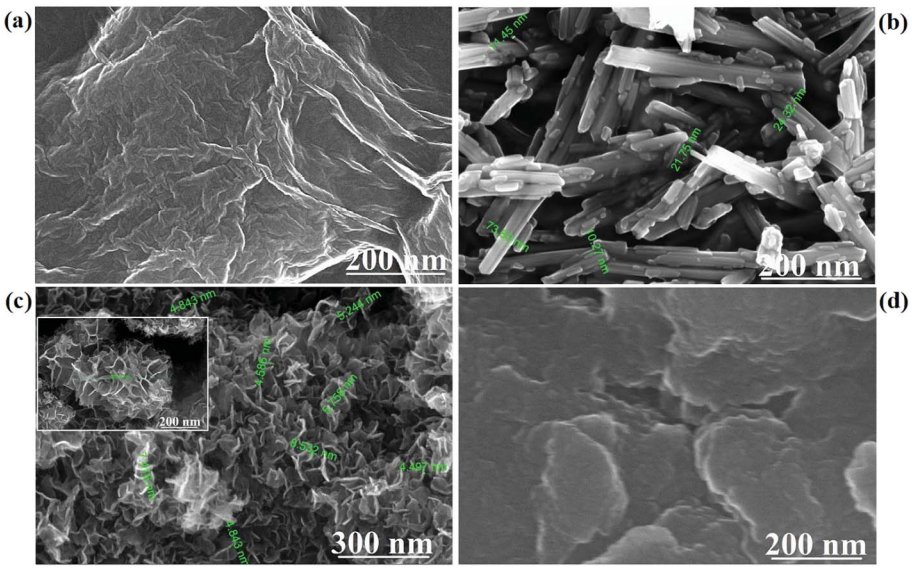

Fig. 1 FESEM images of (a) GO, (b) MnO_2 nanorods, (c) MG nanocomposite and (d) MGP nanocomposite.

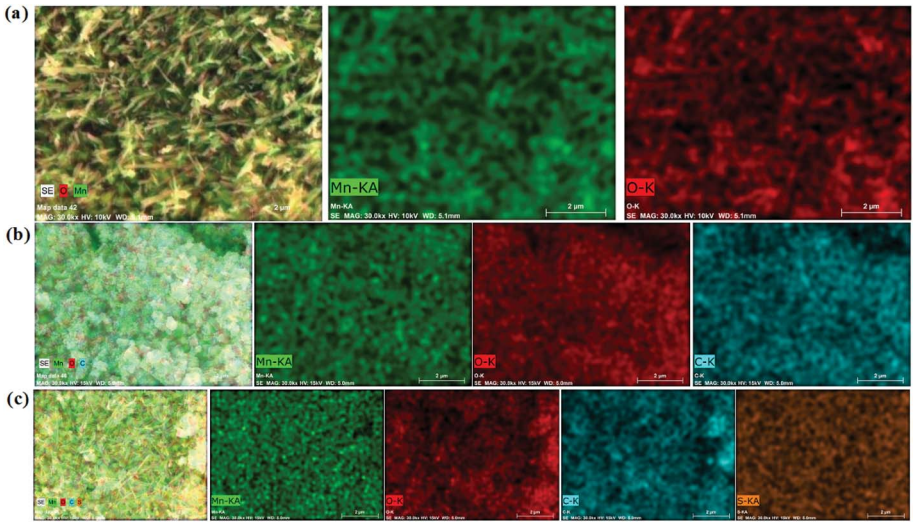

Fig. 2 Elemental mapping of (a) MnO_2, (b) MG nanocomposite and (c) MGP nanocomposite for Mn, O, C and S.

the MG and MGP nanocomposites. In addition to this, a broad peak around 24.51° is observed in the MG nanocomposites, representing rGO and corresponding to (200).[28] In the case of MGP nanocomposites, a broad peak was observed around 26.1°, corresponding to the (020) plane of the backbone of the PEDOT:PSS polymer.[34] It can also be observed that the peak intensity of the MnO_2 nanorods decreased in MGP nanocomposites implying the wrapping of MnO_2/rGO nanocomposite by PEDOT:PSS polymer.[38]

XPS analysis was carried out to study the chemical analysis of the nanocomposites. The survey scan of the GO and MGP nanocomposites is shown in Fig. 3(b), which confirmed the presence of C 1s, O 1s, Mn 2p and S 2p. The high resolution XPS of C 1s of GO is shown in Fig. 3(c). It is deconvoluted into three peaks at 284.8 eV, 286.8 eV and 288.4 eV corresponding to C–C, C–O and C=O, respectively.[38] The intensity of these oxygen functional groups is decreased in the MGP nanocomposites as can be seen from Fig. 3(d), confirming the reduction of GO.[37] Fig. 3(e) shows the high resolution XPS of Mn 2p. It shows two peaks at 642.1 eV and 653.4 eV, corresponding to Mn $2p_{3/2}$ and Mn $2p_{1/2}$, which is in good agreement with energy splitting spectrum of standard MnO_2.[29] The peak to peak separation

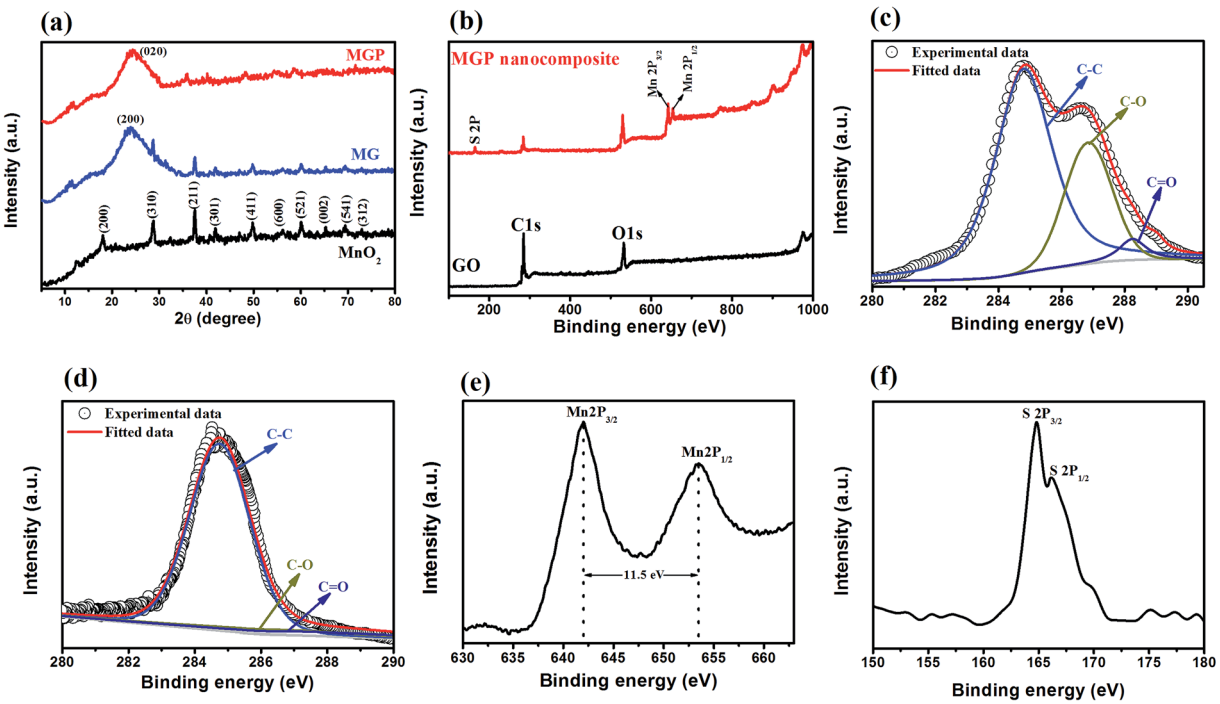

Fig. 3 (a) XRD of nanocomposite along with MnO_2 nanorods; (b) XPS survey scan of GO and the MGP nanocomposite; high resolution XPS of (c) C 1s of GO; (d) C 1s of MGP; (e) Mn 2p of MGP and (f) S 2p of MGP.

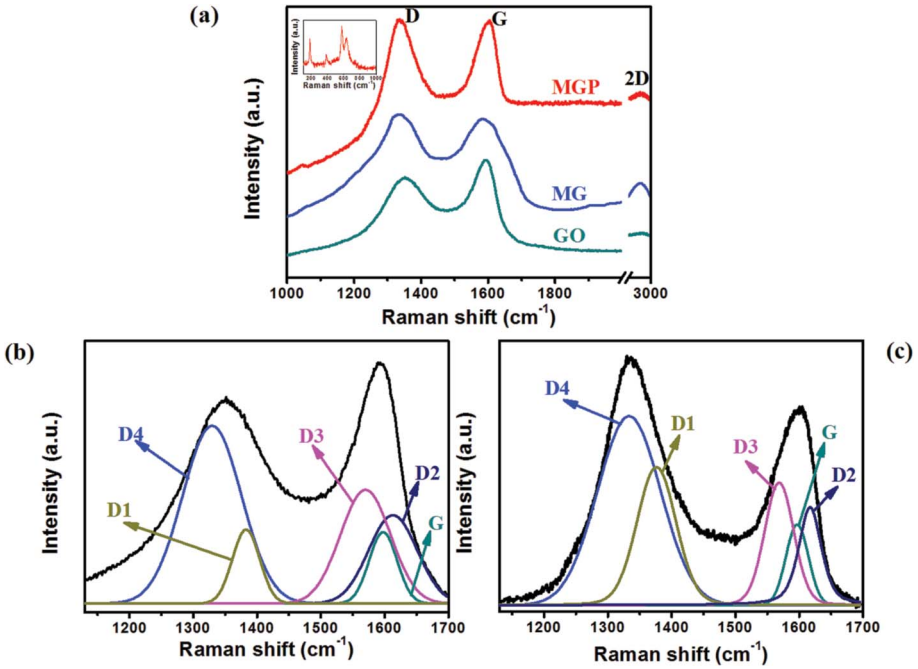

Fig. 4 (a) Raman spectrum of GO, MG nanocomposite and MGP nanocomposite; deconvoluted Raman spectrum of (b) GO and (c) MGP.

between Mn $2p_{3/2}$ and Mn $2p_{1/2}$ is 11.5 eV and is in good agreement with already reported values.[29] The S 2p high resolution XPS spectrum is shown in Fig. 3(f). It shows two peaks at 164.94 eV and 166.14 eV, corresponding to S $2p_{3/2}$ and S $2p_{1/2}$ with peak to peak separation between them as 1.2 eV and is in good agreement with the values reported in the literature.[39]

Fig. 4(a) shows Raman spectra of GO, and the MG and MGP nanocomposites. It can be seen that all the spectra show characteristics D and G bands at 1350 and 1590 cm^{-1}, corresponding to vacancies, edge defects, grain boundaries, and disordered carbon species in graphite layers[40] and an in-plane bond stretching motion of C sp^2 atoms, respectively.[41] The intensity ratio of the D to G band, *i.e.* I_D/I_G, is a measure of the sp^2 domain size of the carbon structure and partially ordered crystal structure of graphene.[40] The I_D/I_G is found to be 0.84 for GO, while it is found to be 1.02 and 1.16 for MG and the MGP nanocomposites, respectively. The increase in I_D/I_G ratio of the nanocomposites compared to GO indicates an increase in disorderness/defects in rGO.[40] As explained by Rusi and Majid, the increment in the D band intensity is due to the combined bands of D1, D2, D3 and D4 in the region 1300–1700 cm^{-1}. The deconvoluted Raman spectra for GO and the MGP nanocomposite are shown in Fig. 4(b) and (c). The deconvoluted bands D1, D2, D3 and D4 correspond to disordered graphitic lattice (graphene layer edges, A_{1g}-symmetry), disordered graphitic lattice (surface graphene layers, E_{2g}-symmetry), amorphous carbon (Gaussian or Lorentzian line shape) and disordered graphitic lattice (A_{1g}-symmetry, polyenes, ionic impurities *etc.*), respectively. The positions of the D1, D2, D3, D4 bands and I_{D_x}/I_G ratios of GO and the MGP nanocomposite are listed in Table 1. The increment in D band intensity is mainly due to the overlapping of D1 and D4 bands in the region 1200–1400 cm^{-1}, indicating an increase in disordered carbon in the graphitic lattice.[40] For the MG and MGP nanocomposites, a broad peak around 2900 cm^{-1} appears, corresponding to 2D graphene, confirming the reduction of GO.[41] The inset of Fig. 4(a) shows the Raman spectrum of MnO_2 of the MGP nanocomposite, showing peaks around 190–380 cm^{-1} and 575–650 cm^{-1}, corresponding to α-MnO_2 (ref. 42) and stretching vibrations of the octahedral MnO_6.[40] Fig. S3† shows the TGA of GO, MnO_2, and the MG and MGP nanocomposites. GO showed an initial weight loss before 200 °C, which is due to the removal of adsorbed water and oxygen functional groups. After 200 °C, GO showed less weight loss to 400 °C and then a sudden weight loss. MnO_2 showed good thermal stability, in good agreement with the literature.[29] The percentages of MnO_2 and rGO in the MG nanocomposite are found to be 13% and 70%, respectively. In the case of the MGP nanocomposite, the percentages of MnO_2, rGO and PEDOT:PSS are found to be 13%, 54% and 17%, respectively.

Table 1 Peak position and I_{D_x}/I_G ratio for the Raman deconvoluted bands of MGP and GO

	Raman shift (cm^{-1})		Ratio (I_{D_x}/I_G)	
Bands	MGP	GO	MGP	GO
D1	1380	1379	1.74	1.04
D2	1618	1612	1.23	1.23
D3	1568	1569	1.56	1.51
D4	1329	1333	2.41	2.39
G	1596	1598	—	—

Fig. 5 shows Nitrogen adsorption–desorption isotherm curves for MnO_2, and the MG and MGP nanocomposites. It can be seen from the figure that the hysteresis loop observed in the relative pressure ranges of 0.76–0.94, 0.8–0.9 and above 0.9 for

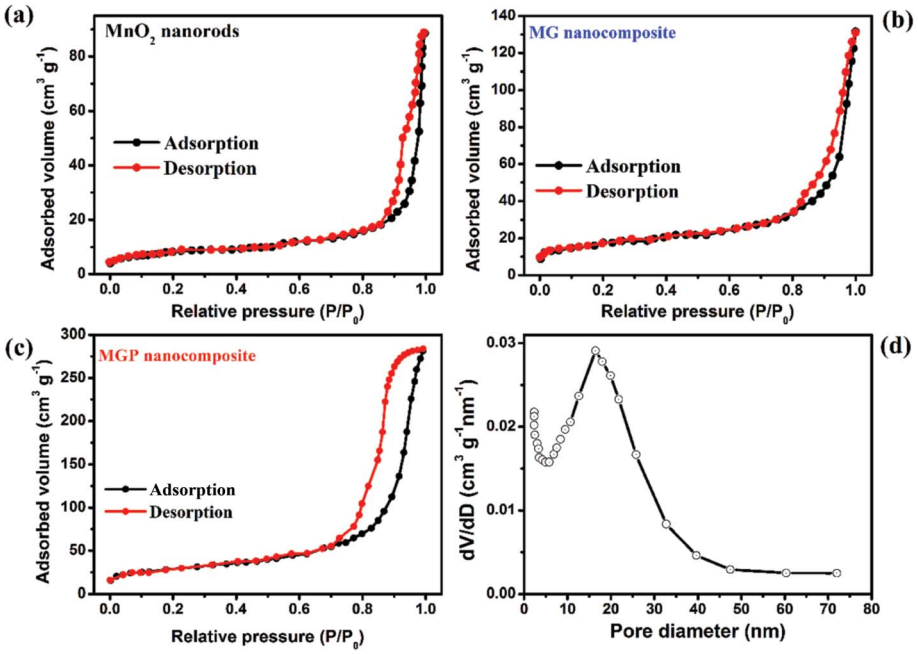

Fig. 5 Nitrogen adsorption–desorption curves for (a) MnO_2, (b) MG nanocomposite, (c) MGP nanocomposite and (d) pores size distribution of the MGP nanocomposite.

Table 2 Surface area and pore volume of MnO_2, and the MG and MGP nanocomposites

Electrode materials	Surface area ($m^2\ g^{-1}$)	Mesoporous volume ($cm^3\ g^{-1}$)	Pore size distribution (nm)
MnO_2 nanorods	58	0.308	3.17
MG	101	0.391	3.42
MGP	208	0.861	7.54

the MGP and MG nanocomposites, and MnO_2, respectively. The width of hysteresis is more for the MGP nanocomposite, indicating that it is more mesoporous than the other samples.[43] The pore size distribution for the MGP nanocomposite is shown in Fig. 5(d), which shows that the mesopore size mainly falls in the 5–30 nm range. The surface area and pore volume for MnO_2, and the MG and MGP nanocomposites are listed in Table 2. From that, the MGP nanocomposite exhibited more surface area, 208 $m^2\ g^{-1}$, and those of the MG nanocomposite and MnO_2 are 101 $m^2\ g^{-1}$ and 58 $m^2\ g^{-1}$, respectively. Also, the MGP nanocomposite showed more pore volume than the MG nanocomposite and MnO_2 nanorods. The high surface area and high mesoporous nature of the MGP nanocomposite may result in more ionic transportation through the material, leading to enhancement in the supercapacitance performance.

Fig. 6(a) shows typical cyclic voltammograms of MnO_2, and the MG and MGP nanocomposites in the potential window of 0 to 1.1 V at a scan rate of 100 mV s^{-1} carried out in acetonitrile solution containing 1 M $LiClO_4$ electrolyte. All the samples showed asymmetrical CV curves that can be attributed to the combined double-layer and pseudocapacitive contributions to the total capacitance. It is observed that the MGP nanocomposites exhibited a large area under the CV curve, indicating superior supercapacitance behaviour among all. The plausible electrochemical reaction steps governed by the MnO_2 are as follows.

$$(MnO_2)_{surface} + Li^+ + e^- \rightarrow (MnO_2^-Li^+)_{surface} \quad (2)$$

$$MnO_2^- + Li^+ + e^- \rightarrow MnOOLi \quad (3)$$

The above equations indicate that the diffusion of Li^+ into the interior of MnO_2 and charge transfer has a significant effect on the rate capability. The relation between the peak current and the CV scan rate is given by the following equation.[44]

$$i_p = 2.69 \times 10^5 n^{3/2} A D^{1/2} C \nu^{1/2} \quad (4)$$

where 'i_p' is the peak current (A), 'n' is the number of electrons transferred per step during oxidation, 'A' is the geometrical area of electrode, 'D' is the diffusion coefficient of Li^+ ions, 'C' is the concentration of Li^+ ions and 'ν' is the CV scan rate. The diffusion coefficients calculated using eqn (4) for MnO_2, and the MG and MGP nanocomposites are found to be 0.05×10^{-11} $cm^2\ s^{-1}$, 0.24×10^{-11} $cm^2\ s^{-1}$ and 0.81×10^{-11} $cm^2\ s^{-1}$, respectively. It can be observed that the MGP nanocomposite showed the largest diffusion coefficient of all due to a good dispersion of the MnO_2 nanorods and an enhanced conducive network between the MnO_2 nanorods decorated on the rGO sheet and PEDOT:PSS polymer, leading to an enhanced supercapacitance performance.[45] Fig. 6(b) shows the CV curves for the MGP nanocomposite in a potential window from 0 to 1.1 V at

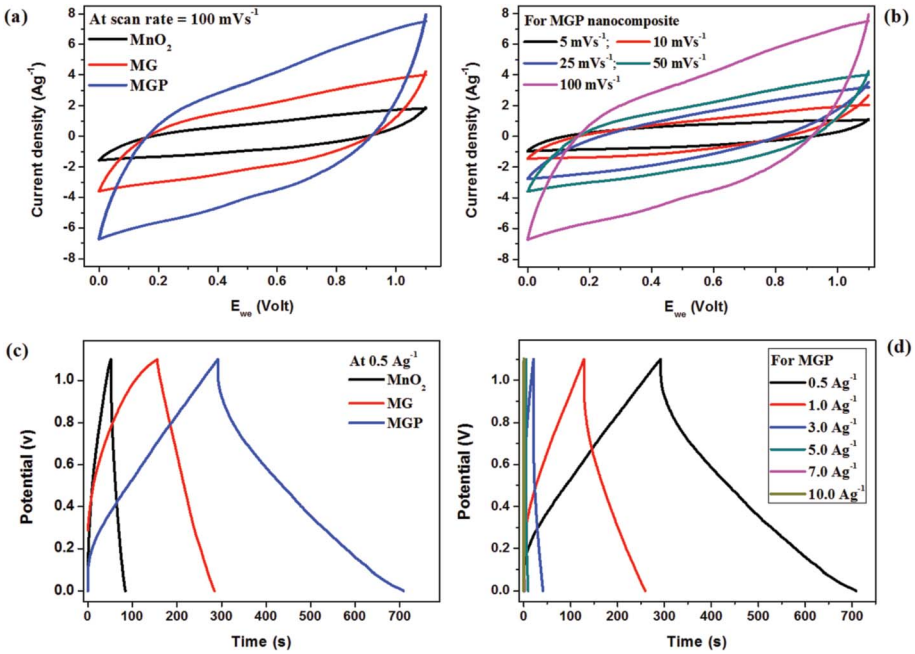

Fig. 6 Cyclic voltammograms of (a) all the samples at a scan rate of 100 mV s^{-1} and (b) the MGP nanocomposite at different scan rates; charge–discharge curves of (c) all the samples at a current density 0.5 A g^{-1} and (d) the MGP nanocomposite at different current densities. All measurements were done in acetonitrile solution containing 1 M $LiClO_4$.

different scan rates. It can be observed from Fig. 6(b) that the current density increases with an increase in the scan rate, indicating its excellent capacitance behaviour.

Fig. 6(c) shows the galvanostatic charge–discharge for MnO_2, and the MG and MGP nanocomposites at a current density of 0.5 A g^{-1}. It is observed from the figure that the all the samples showed nearly triangular shape charge–discharge curves, indicating the electric double layer capacitance behaviour. Also, the ternary nanocomposite showed an ideal capacitive behaviour with very sharp responses and a small internal resistance (IR) drop. The specific capacitance (C_s) of all the samples was calculated using the following equation,[46,47]

$$C_s = \frac{i \times \Delta t}{m \times \Delta V} \quad (5)$$

where i is the applied current, Δt is the time of discharge, m is the mass of active material (0.3 mg), and ΔV is the voltage drop upon discharging. The specific capacitance values for MnO_2, and the MG and MGP nanocomposites are found to be 55, 199 and 633 F g^{-1}, respectively, at a current density of 0.5 A g^{-1}. It can be seen that the MGP nanocomposite showed more specific capacitance than MnO_2 and the MG nanocomposite. The enhanced specific capacitance of the MGP nanocomposite is due to a synergetic effect between the individual three components. The MnO_2 nanorods that decorate rGO may prevent the restacking of rGO sheets, resulting in a high surface area, which is also supported by BET analysis, leading to an increase in electrode/electrolyte contact areas. The other reason may be due to the addition of PEDOT:PSS, which might have reduced the agglomeration of MnO_2/rGO results in the higher surface area

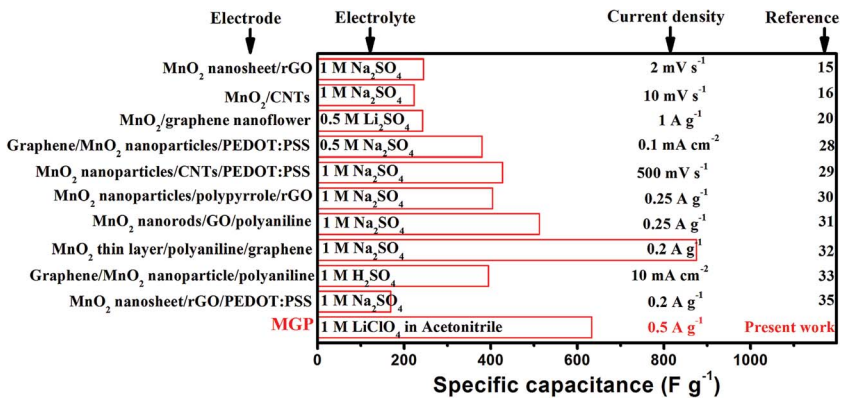

Chart 1 Comparison of the specific capacitance of the present work (MGP nanocomposite) with reported electrode materials.

and porosity provided by them. Also, PEDOT:PSS might have provided numerous active sites for efficient faradic redox reaction and, also, restricts the dissolution and aggregation of MnO_2 with the help of rGO, which possibly keeps the MnO_2/rGO part well separated and provides more interfaces for the charge storage.[29,32,36,48] The obtained specific capacitance for the MGP nanocomposite has been compared with MnO_2, rGO and conducting polymer based binary and tertiary nanocomposites reported in the literature, as shown in bar Chart 1.[15,16,20,28–33,35] Fig. 6(d) shows the galvanostatic charge–discharge curves for the MGP nanocomposite carried out at different current densities from 0.5 A g^{-1} to 10 A g^{-1}.

Furthermore, capacitance retention is an important parameter for the practical application of electrode materials. Therefore, the cycling stability of the MGP nanocomposite has been carried out at 1 A g^{-1} for 5000 cycles. The capacitance retention (%) for the MGP nanocomposite over 5000 cycles is shown in Fig. 7(a). Interestingly, it can be seen that the MGP nanocomposite retained the same specific capacitance even after 5000 cycles, *i.e.* it showed 100% capacitance retention (%), which is excellent in its class. This excellent capacitance retention may be due to the addition of the PEDOT:PSS polymer, which provides support to the MnO_2 nanorods and also restricts the dissolution and aggregation of MnO_2 with the help of rGO, which possibly keeps the MnO_2/rGO part well separated and provides more interfaces for charge storage.

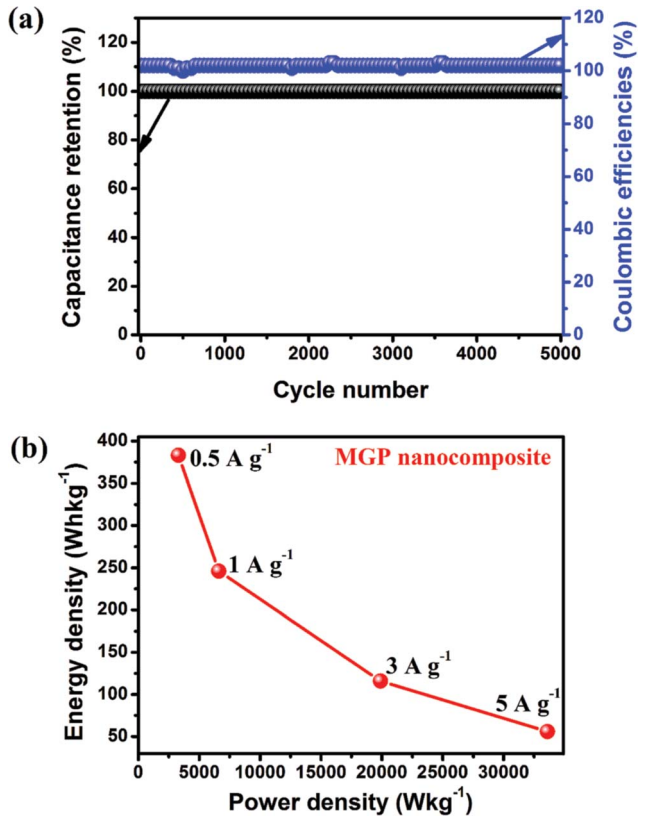

Fig. 7 (a) Capacitance retention (%) and coulombic efficiency of the MGP nanocomposite over 5000 cycles at a current density of 1 A g^{-1}; (b) Ragone plot for the MGP nanocomposite.

Coulombic efficiency (η) was calculated using eqn (6) and is plotted in Fig. 7(a). It can be observed from the figure that the coulombic efficiency showed an almost constant value over 300 cycles without any fluctuations, suggesting little energy dissipation during the charge–discharge process. The energy density (d_E) and power density (d_P) of MnO_2, and the MG and MGP nanocomposites were calculated using eqn (7) and (8)[48,49]

$$\eta = \frac{t_D}{t_C} \times 100\% \quad (6)$$

$$d_E = \frac{1}{2} C_s (\Delta V)^2 \quad (7)$$

$$d_P = \frac{d_E}{\Delta t} \quad (8)$$

where t_C is the charging time, t_D is the discharge time and C_s is the specific capacitance. The Ragone plot, *i.e.* plot of energy density *versus* power density in the current density range 0.5–5 A g^{-1} for the MGP nanocomposite, is shown in Fig. 7(b). It can be observed that the energy density decreased with an increase in the power density, which is in agreement with results reported in the literature.[36]

Electrochemical impedance spectroscopy (EIS) was used to study the charge transfer and transport mechanism for MnO_2, and the MG and MGP nanocomposites. Fig. 8 shows Nyquist plots for MnO_2, and the MG and MGP nanocomposites carried out in acetonitrile solution containing 1 M $LiClO_4$ electrolyte in the frequency range 6 MHz to 200 mHz. It can be seen from the figure that all the curves showed a semicircle at higher frequencies and nearly a straight line at lower frequencies. Among all, the MGP nanocomposite showed the lowest semicircle, suggesting the lowest resistance, which in turn indicates the highest capacitance, in agreement with the galvanostatic charge–discharge analysis. In addition to this, the EIS spectra were analysed using a semi quantitative fitting program supplied along with the BioLogic potentiostat (model: SP 300) on the basis of the Randles equivalent circuit modelling, shown in the inset (Fig. 8(b)) of Fig. 8. The Randles equivalent circuit

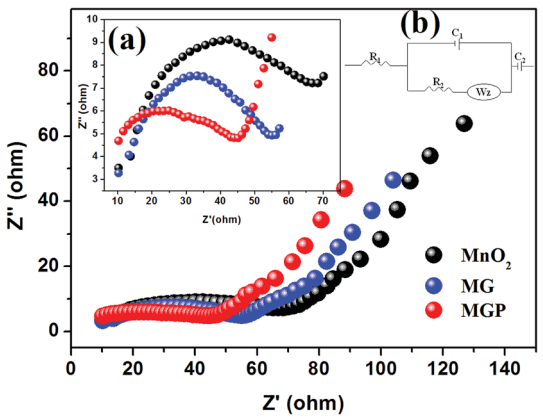

Fig. 8 Nyquist plots for MnO_2, and the MG and MGP nanocomposites carried out in acetonitrile solution containing 1 M $LiClO_4$; inset shows (a) enlarged Nyquist plots at a higher frequency range, and (b) equivalent electrical circuit composed of five elements.

Table 3 Electrochemical parameters of different electrode materials obtained from impedance analysis based upon the proposed Randles circuit

Electrode material	R_1 (Ω)	R_2 (Ω)	C_1 (mF)	C_2 (F)	W_Z (Ω $s^{-0.5}$)
MnO_2 nanorods	1.75	0.56	2.31	0.076	0.65
MG	1.29	0.25	5.72	0.105	0.82
MGP	0.97	0.16	8.19	0.389	0.98

consists of five elements, internal resistance (R_1), electrical double layer capacitance at the interface of electrode and electrolyte (C_1), charge transfer resistance (R_2), Warburg impedance (W_Z) and pseudocapacitance (C_2), which is used to account for the faradic reaction. These values were calculated qualitatively from the fittings (mean error of modulus $\sim$ 0.4%) of experimental EIS spectra and are tabulated in Table 3. It can be observed that the internal resistance (R_1), *i.e.* intrinsic resistance of the MGP nanocomposite, is less compared to MnO_2 and the MG nanocomposite. This is due to the development of an internal mesoporous nanorod structure during the MGP nanocomposite synthesis. The lower value of the charge transfer resistance (R_2) for the MGP nanocomposite compared to MnO_2 and the MG nanocomposite indicates a significant pore size distribution in the MGP nanocomposite. This helps to reduce the intrinsic resistance (R_1) *via* the development of a large number of mesoporous structures. This results in an increase in the kinetics of electron transfer through the redox process, leading to an increase in pseudocapacitance (C_2) in the nanocomposite. Moreover, the influence of pseudocapacitance is quite larger than the electrical double layer capacitance (C_1), as the conducting polymer PEDOT:PSS itself behaves as a redox system along with MnO_2. The lower value of Warburg impedance is attributed to the diffusion of electrolyte in the mesoporous structure of the electrode material at a lower frequency.

Conclusions

The synthesized MGP nanocomposite demonstrated an enhanced supercapacitance performance compared to MnO_2 and the MG nanocomposite. The specific capacitance of the MGP nanocomposite was found to be 633 F g^{-1} at a current density of 0.5 A g^{-1} with 100% capacitance retention even after 5000 cycles. The enhanced specific capacitance of the MGP nanocomposite is due to the synergetic effect of the individual components and also the addition of the PEDOT:PSS conducting polymer is an important factor which may provide numerous active sites for faradic redox reactions as well as support the MnO_2 nanorods. Overall, we can conclude that the MGP nanocomposite is an excellent material for supercapacitance application and shows an ultra-high stability even after long term cyclic stability.

Acknowledgements

One of the authors, KH, acknowledges a Research Fellowship from the Endeavour Australia-India Education Council.

References

1 T. Guo, M. S. Yao, Y. H. Lin and C. W. Nan, *CrystEngComm*, 2015, **17**, 3551–3585.
2 C. Yuan, H. B. Wu, Y. Xie and X. W. Lou, *Angew. Chem., Int. Ed.*, 2014, **53**, 1488–1504.
3 A. Gonzalez, E. Goikolea, J. A. Barrena and R. Mysyk, *Renewable Sustainable Energy Rev.*, 2016, **58**, 1189–1206.
4 M. A. Sakka, H. Gualous, J. V. Mierlo and H. Culcu, *J. Power Sources*, 2009, **194**, 581–587.
5 W. K. Chee, H. N. Lim, Z. Zainal, N. M. Huang, I. Harrison and Y. Andou, *J. Phys. Chem. C*, 2016, **120**, 4153–4172.
6 X. Liu, C. Chen, Y. Zhao and B. Jia, *J. Nanomater.*, 2013, **2013**, 736375.
7 H. Wang, Z. Lu, D. Qian, Y. Li and W. Zhang, *Nanotechnology*, 2007, **18**, 115616.
8 D. Belanger, T. Brousse and J. W. Long, *Electrochem. Soc. Interface*, 2008, **17**, 49–52.
9 G. Yu, L. Hu, M. Vosgueritchian, H. Wang, X. Xie, J. R. McDonough, X. Cui, Y. Cui and Z. Bao, *Nano Lett.*, 2011, **11**, 2905–2911.
10 Y. Yu, B. Zhang, Y. B. He, Z. D. Huang, S. W. Oh and J. K. Kim, *J. Mater. Chem. A*, 2013, **1**, 1163–1170.
11 D. Chen, H. Feng and J. Li, *Chem. Rev.*, 2012, **112**, 6027–6053.
12 Y. B. Tan and J. M. Lee, *J. Mater. Chem. A*, 2013, **1**, 14814–14843.
13 S. Thakur and N. Karak, *Carbon*, 2015, **94**, 224–242.
14 D. Chen, H. Feng and J. Li, *Chem. Rev.*, 2012, **112**, 6027–6053.
15 Y. Zhao, Y. Meng, H. Wu, Y. Wang, Z. Wei, X. Li and P. Jiang, *RSC Adv.*, 2015, **5**, 90307–90312.
16 H. Xia, Y. Wang, J. Lin and L. Lu, *Nanoscale Res. Lett.*, 2012, **7**, 33.
17 P. Ning, X. Duan, X. Ju, X. Lin, X. Tong, X. Pan, T. Wang and Q. Li, *Electrochim. Acta*, 2016, **210**, 754–761.
18 R. T. Vinny, K. Chaitra, K. Venkatesh, N. Nagaraju and N. Kathyayini, *J. Power Sources*, 2016, **309**, 212–220.
19 W. Ma, S. Chen, S. Yang, W. Chen, Y. Cheng, Y. Guo, S. Peng, S. Ramakrishna and M. Zhu, *J. Power Sources*, 2016, **306**, 481–488.
20 J. Liu, Y. Zhang, Y. Li, J. Li, Z. Chen, H. Feng, J. Li, J. Jiang and D. Qian, *Electrochim. Acta*, 2015, **173**, 148–155.
21 N. Zhang, C. Fu, D. Liu, Y. Li, H. Zhou and Y. Kuang, *Electrochim. Acta*, 2016, **210**, 804–811.
22 G. A. Snook, P. Kao and A. S. Best, *J. Power Sources*, 2011, **196**, 1–12.
23 V. Singh, S. Arora, M. Arora, V. Sharma and R. P. Tandon, *Semicond. Sci. Technol.*, 2014, **29**, 045020.
24 C. Yin, C. Yang, M. Jiang, C. Deng, L. Yang, J. Li and D. Qian, *Appl. Mater. Interfaces*, 2016, **8**, 2741–2752.
25 T. Cheng, Y. Z. Zhang, J. D. Zhang, W. Y. Lai and W. Huang, *J. Mater. Chem. A*, 2016, **4**, 10493–10499.
26 C. Yeon, G. Kim, J. W. Lim and S. J. Yun, *RSC Adv.*, 2017, **7**, 5888–5897.
27 D. Antiohos, G. Folkes, P. Sherrell, S. Ashraf, G. G. Wallace, P. Aitchison, A. T. Harris, J. Chen and A. I. Minett, *J. Mater. Chem.*, 2011, **21**, 15987–15994.

28 G. Yu, L. Hu, N. Liu, H. Wang, M. Vosgueritchian, Y. Yang, Y. Cui and Z. Bao, *Nano Lett.*, 2011, **11**, 4438–4442.
29 Y. Hou, Y. Cheng, T. Hobson and J. Liu, *Nano Lett.*, 2010, **10**, 2727–2733.
30 G. Han, Y. Liu, E. Kan, J. Tang, L. Zhang, H. Wang and W. Tang, *RSC Adv.*, 2014, **4**, 9898–9904.
31 G. Han, Y. Liu, L. Zhang, E. Kan, S. Zhang, J. Tang and W. Tang, *Sci. Rep.*, 2014, **4**, 4824.
32 C. Pan, H. Gu and L. Dong, *J. Power Sources*, 2016, **303**, 175–181.
33 B. Mu, W. Zhang, S. Shao and A. Wang, *Phys. Chem. Chem. Phys.*, 2014, **16**, 7872–7880.
34 H. Li, Y. He, V. Pavlinek, Q. Cheng, P. Sahab and C. Li, *J. Mater. Chem. A*, 2015, **3**, 17165–17171.
35 D. Yan, Y. Liu, Y. Li, R. Zhuo, Z. Wu, P. Ren, S. Li, J. Wang, P. Yan and Z. Geng, *Mater. Lett.*, 2014, **127**, 53–55.
36 K. Hareesh, B. Shateesh, R. P. Joshi, S. S. Dahiwale, V. N. Bhoraskar, S. K. Haram and S. D. Dhole, *Electrochim. Acta*, 2016, **201**, 106–116.
37 Y. Zhou, Q. Bao, L. A. L. Tang, Y. Zhong and K. P. Loh, *Chem. Mater.*, 2009, **21**, 2950–2956.
38 W. Wang, Q. Hao, W. Lei, X. Xia and X. Wang, *J. Power Sources*, 2014, **269**, 250–259.
39 L. Zhang, L. Ji, P. A. Glans, Y. Zhang, J. Zhu and J. Guo, *Phys. Chem. Chem. Phys.*, 2012, **14**, 13670–13675.
40 Rusi and S. R. Majid, *Sci. Rep.*, 2015, **5**, 16195.
41 L. M. Malard, M. A. Pimenta, G. Dresselhaus and M. S. Dresslhaus, *Phys. Rep.*, 2009, **473**, 51–87.
42 Y. Wang, H. Guan, S. Du and Y. Wang, *RSC Adv.*, 2015, **5**, 8979–88988.
43 E. Raymundo-Pinero, V. Khomenk, E. Frackowiak and F. Beguin, *J. Electrochem. Soc.*, 2005, **152**, A229–A235.
44 N. Ding, J. Xu, Y. X. Yao, G. Wegner, X. Fang, C. H. Chen and I. Lieberwirth, *Solid State Ionics*, 2009, **180**, 222–225.
45 L. L. Zhang, S. Duan, X. L. Yang, G. Peng, G. Liang, Y. H. Huang, Y. Jiang, S. B. Ni and M. Li, *Appl. Mater. Interfaces*, 2015, **3**, 12304–12309.
46 H. Fan, L. Quan, M. Yuan, S. Zhu, K. Wang, Y. Zhong, L. Chang, H. Shao, J. Wang, J. Zhang and C.-N. Cao, *Electrochim. Acta*, 2016, **188**, 222–229.
47 X. Li, C. Zhang, S. Xin, Z. C. Yang, Y. Li, D. Zhang and P. Yao, *Appl. Mater. Interfaces*, 2016, **8**, 21373–21380.
48 M. M. Islam, A. T. Chidembo, S. H. Aboutalebi, D. Cardillo, H. K. Liu, K. Konstantinov and S. X. Dou, *Frontiers in Energy Research*, 2014, **2**, 31.
49 P. Sen and A. De, *Electrochim. Acta*, 2010, **55**, 4677–4684.